

Microscopic-Mamba: Revealing the Secrets of Microscopic Images with Just 4M Parameters

Shun Zou^{1,5*}, Zhuo Zhang^{2*}, Yi Zou³, Guangwei Gao^{4,5†}

¹College of Artificial Intelligence, Nanjing Agricultural University, Nanjing, China

²College of Computer Science and Technology, National University of Defense Technology, Changsha, China

³School of Automation and Electronic Information, Xiangtan University, Xiangtan, China

⁴Institute of Advanced Technology, Nanjing University of Posts and Telecommunications, Nanjing, China

⁵Provincial Key Laboratory for Computer Information Processing Technology, Soochow University, Suzhou, China
zs@stu.njau.edu.cn, zhangzhuo@nudt.edu.cn, 202205570112@smail.xtu.edu.cn, csggao@gmail.com

Abstract—In the field of medical microscopic image classification (MIC), CNN-based and Transformer-based models have been extensively studied. However, CNNs struggle with modeling long-range dependencies, limiting their ability to fully utilize semantic information in images. Conversely, Transformers are hampered by the complexity of quadratic computations. To address these challenges, we propose a model based on the Mamba architecture: Microscopic-Mamba. Specifically, we designed the Partially Selected Feed-Forward Network (PSFFN) to replace the last linear layer of the Visual State Space Module (VSSM), enhancing Mamba’s local feature extraction capabilities. Additionally, we introduced the Modulation Interaction Feature Aggregation (MIFA) module to effectively modulate and dynamically aggregate global and local features. We also incorporated a parallel VSSM mechanism to improve inter-channel information interaction while reducing the number of parameters. Extensive experiments have demonstrated that our method achieves state-of-the-art performance on five public datasets. Code is available at <https://github.com/zs1314/Microscopic-Mamba>

Index Terms—Microscopic images, State Space Model, Microscopic-Mamba

I. INTRODUCTION

Microscopic imaging technology is vital in medicine, serving as an indispensable tool for modern medical research and clinical diagnosis [1]. By classifying microscopic images, medical researchers can observe structural and dynamic changes at the tissue, cell, and molecular levels, gaining a deeper understanding of disease mechanisms and pathological processes [2]. Typical microscopic image classification (MIC) tasks rely heavily on specialists, consuming significant manpower and time, leading to inconsistent and less accurate results. These highlight the need for automated microscopic image recognition.

Recently, convolutional neural networks (CNNs) and Vision Transformers (ViTs) have been widely applied in MIC [3]–[6]. However, CNN-based models are limited by their local receptive fields, which significantly hinders their ability to capture long-range information. While ViT-based models excel

at global modeling, their attention mechanism’s quadratic complexity in long-sequence modeling imposes a high computational burden. This burden neglects the computational constraints of real-world medical environments [7]. Although some studies have proposed methods to reduce the computational complexity of ViTs [8]–[10] and have combined ViTs with CNNs to create lightweight models [11] [12], this is achieved at the cost of sacrificing ViTs’ ability to capture global information in self-attention. Therefore, a new architecture is urgently needed that can effectively capture both global and local features while maintaining linear complexity.

State Space Models (SSMs) have recently garnered significant interest [13]–[15]. Building on classical SSM research, modern SSMs like Mamba [16] not only establish long-range dependencies but also exhibit linear complexity related to input size, making Mamba a strong competitor to CNNs and ViTs in lightweight MIC applications. Researchers have already applied Mamba to the medical imaging field, for example Segmamba [17] creating SSM-CNN hybrid models to effectively model pixel-level long-range dependencies. T-Mamba [18] integrates shared positional encoding and frequency-based features into Vision Mamba to address limitations in spatial position retention and feature enhancement in the frequency domain. Contrastive Masked Vim Autoencoder [19] is a new method for 3D multi-modal data representation learning, enhancing Alzheimer’s diagnosis by improving multi-modal alignment and reconstruction through contrastive learning.

However, when directly applied to MIC tasks, this promising architecture’s accuracy does not match its efficiency. Unlike other visual tasks with distinct target features, MIC requires capturing both global context and local fine-grained features. Therefore, this paper proposes an enhanced Mamba architecture for MIC, advancing its application in MIC tasks.

In summary, our contributions are as follows: (1) We proposed a lightweight hybrid architecture Microscopic-Mamba. It combines Mamba’s advantages in learning global features and CNN’s strength in extracting local features. To our knowledge, this is the first application of Mamba in MIC tasks, providing a new benchmark and reference for future efficient MIC explorations. (2) We propose a novel dual-branch Hybrid-Conv-SSM Block, which includes a Conv branch and an

*Equal Contribution.

†Corresponding author.

This work was supported in part by the Open Fund Project of Provincial Key Laboratory for Computer Information Processing Technology (Soochow University) under Grant KJS2274.

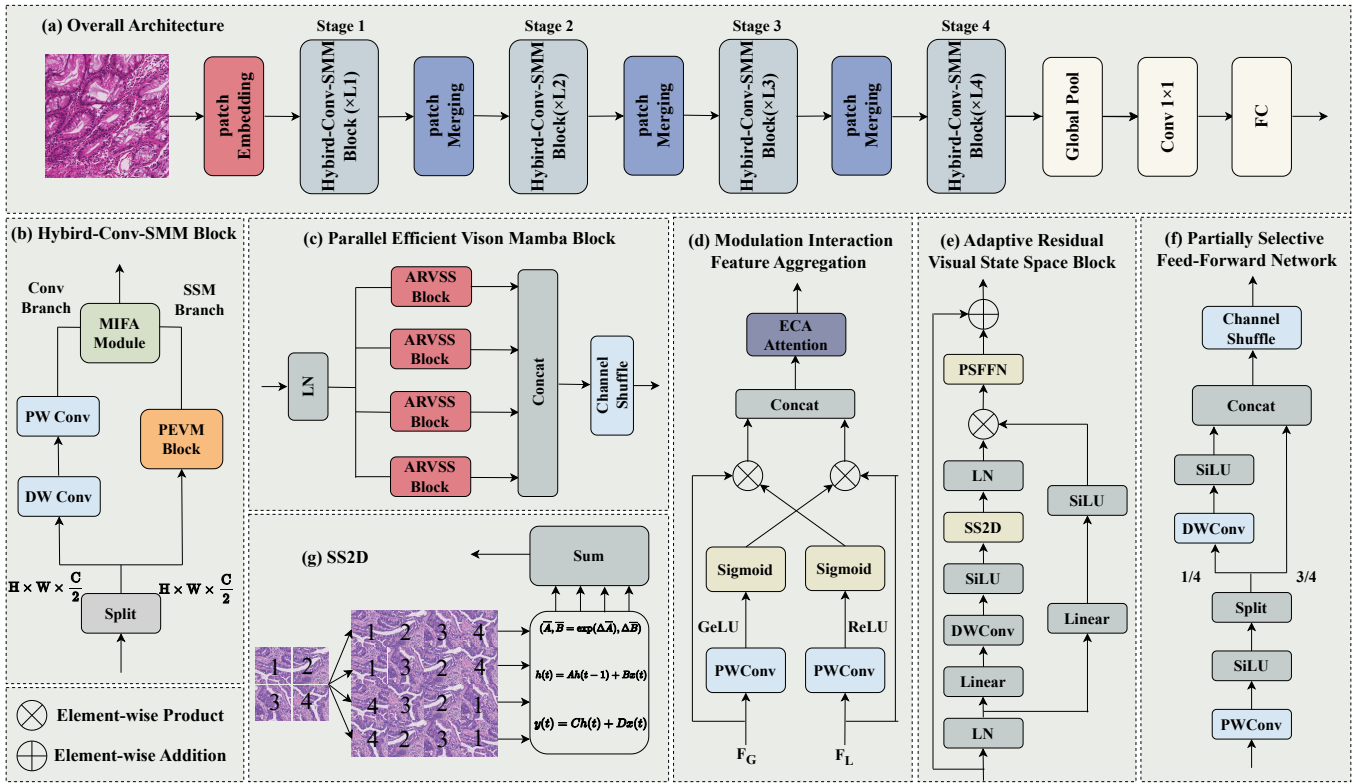


Fig. 1. Overall and detailed architecture of the Microscopic-Mamba.

SSM branch, with the Adaptive Residual Visual State Space (ARVSS) Block at the core of the SSM branch. We introduced a Partially Selected Feed-Forward Network (PSFFN) as a superior replacement for the final linear layer in the Visual State Space Module (VSSM), enhancing Mamba’s local information perception capabilities. To further reduce model parameters, we incorporated a parallel VSSM mechanism. Additionally, we proposed the Modulation Interaction Feature Aggregation (MIFA) module to effectively aggregate global and local information. (3) Our extensive experiments on five open-source public microscopic image datasets demonstrated that Microscopic-Mamba outperforms current state-of-the-art methods while maintaining lower parameters and computational complexity.

II. METHOD

A. Overall Architecture

Figure 1 (a) shows the overall architecture of the Microscopic-Mamba. Specifically, it includes four stages composed of stacked Hybrid-Conv-SMM Blocks. Additionally, each stage has an embedding or merging layer before it, used for spatial downsampling and channel expansion. We applied a global average pooling layer to the final output and sent it to a linear classification head.

Hybrid-Conv-SMM Block. The Hybrid-Conv-SMM Block is the core component of Microscopic-Mamba. As shown in Figure 1 (b), it has a dual-branch structure consisting of an SSM

branch and a Conv branch. It uses channel splitting to divide the feature map into two groups, which are then processed by the Conv branch and the SSM branch respectively. The Conv branch, composed of depth-wise separable convolution (DW-Conv) and point-wise convolution (PWConv), extracts local information. The SSM branch, made up of Parallel Efficient Vision Mamba (PEVM) blocks, captures global contextual information. Finally, our proposed Modulation Interaction Feature Aggregation (MIFA) module aggregates these two types of information, completing the global-local feature fusion.

B. Parallel Efficient Vision Mamba Block

As shown in Figure 1 (c), the Parallel Efficient Vision Mamba (PEVM) Block consists of a layer normalization (LN) layer and four Adaptive Residual Visual State Space (ARVSS) blocks. Previous research has shown that parallel networks can help reduce model parameters without losing accuracy. Specifically, the input X_G passes through an LN layer, splitting the feature map into four groups along the channel: X_{G1} , X_{G2} , etc. These groups are processed in parallel by the ARVSS blocks, resulting in Map_{G1} , Map_{G2} , etc. Finally, concatenate these feature maps along the channels. Then, perform Channel Shuffle to enhance information exchange across modules, resulting in the output F_G .

Adaptive Residual Visual State Space Block. Figure 1 (e) describes the ARVSS Block. The input Map_x is split into

TABLE I

COMPARISON WITH STATE-OF-THE-ART METHODS ON FIVE PUBLIC DATASETS. THE BEST RESULTS ARE HIGHLIGHTED IN **BOLD FONTS**. “↑” AND “↓” INDICATE THAT LARGER OR SMALLER IS BETTER.

Method	Year	GMACs ↓	Params ↓	RPE Data		MHIST		SARS		TissueMnist		MedFM Colon		
				OA ↑	AUC ↑	OA ↑	AUC ↑	OA ↑	AUC ↑	OA ↑	AUC ↑	OA ↑	AUC ↑	
CNNs	ConvNext-tiny [20]	CVPR2022	4.49	28.69	86.06	97.96	77.34	84.24	96.88	99.46	66.47	92.07	94.56	98.71
	ConvNext-small	CVPR2022	8.73	50.22	85.44	98.02	76.55	84.12	96.77	99.42	69.22	93.21	87.36	95.05
	RepVit-m1_0 [21]	CVPR2024	1.13	6.85	87.60	98.15	69.10	71.32	96.62	99.42	67.54	92.45	97.45	99.63
	RepVit-m1_1	CVPR2024	1.37	8.29	85.71	98.06	76.70	80.90	97.24	99.56	67.47	92.41	86.41	93.60
	Mobileone-s0 [22]	CVPR2023	1.10	5.29	86.79	98.28	67.83	60.04	96.03	99.17	63.20	90.34	89.26	95.97
	Mobileone-s2	CVPR2023	1.35	7.88	85.71	98.16	70.68	73.07	96.61	99.33	62.66	90.11	87.76	94.62
	Mobileone-s3	CVPR2023	1.96	10.17	86.52	98.24	70.69	73.44	97.08	99.47	66.55	92.05	89.31	95.78
ViTs	PVT-smal [23]	ICCV2021	3.71	24.49	85.44	98.13	73.69	80.11	96.12	99.16	68.60	92.88	97.80	99.81
	PVT-medium	ICCV2021	6.49	44.21	87.33	98.19	80.82	87.72	96.61	99.31	69.17	93.14	97.25	99.57
	MpVit-tiny [24]	CVPR2022	1.84	5.84	87.87	98.11	81.30	87.37	96.93	99.43	70.63	93.79	98.05	99.83
	MpVit-small	CVPR2022	5.32	22.89	85.44	97.95	80.19	86.57	97.02	99.52	70.47	93.73	95.20	98.51
	Twins-small [25]	NIPS2021	3.71	24.11	88.14	98.24	78.76	86.15	96.61	99.40	67.80	92.55	97.45	99.65
	Twins-base	NIPS2021	6.49	43.83	86.79	98.40	81.77	88.93	96.75	99.43	68.25	92.82	93.31	98.29
	Vit-tiny [26]	ICLR2021	1.26	5.71	86.52	97.50	74.33	79.33	96.01	99.18	58.50	87.80	96.15	99.38
	Vit-small	ICLR2021	4.62	22.04	86.54	97.76	75.59	80.94	95.84	99.20	64.36	90.94	92.21	97.63
Vit-base	ICLR2021	17.6	86.54	86.24	97.25	75.44	82.59	96.43	99.37	65.86	91.73	94.61	94.60	
Hybrid-CNN-ViT	FastVit-sa24 [27]	ICCV2023	2.94	21.55	85.44	98.07	78.61	84.04	96.95	99.43	68.60	92.92	98.65	99.89
	FastVit-ma36	ICCV2023	6.07	44.07	88.14	98.08	81.93	85.55	96.95	99.45	68.79	93.00	94.31	98.43
	SwiftFormer-S [28]	ICCV2023	1.01	5.64	85.44	98.04	81.62	90.16	96.88	99.45	69.57	93.40	94.91	98.77
	SwiftFormer-L1	ICCV2023	1.62	11.29	86.52	98.02	81.93	88.47	97.21	99.54	70.59	93.66	95.45	98.92
	SwiftFormer-L3	ICCV2023	4.05	27.47	86.25	98.04	82.25	89.95	97.28	99.53	70.55	93.58	96.15	99.27
	Uniformer-small [29]	ICLR2022	3.46	21.55	86.25	98.13	82.57	89.96	96.79	99.45	71.91	94.27	97.80	99.71
	Uniformer-base	ICLR2022	7.81	49.78	88.14	98.41	81.77	89.08	97.22	99.49	72.06	94.08	95.80	99.15
	SMT-s [30]	ICCV2023	4.72	22.55	83.99	93.73	83.99	89.73	96.93	99.46	71.74	94.33	98.25	99.84
	SMT-b	ICCV2023	7.81	32.04	87.87	98.10	86.05	91.04	96.90	99.45	69.27	93.36	97.85	99.73
	Mambas	Medmamba-s [31]	Arxiv2024	2.75	19.39	86.52	98.17	81.62	87.04	97.01	99.23	69.18	93.12	97.95
Medmamba-b		Arxiv2024	6.16	40.88	86.79	98.02	77.97	85.20	97.30	99.51	69.11	93.18	95.70	98.94
VMamba-t [32]		ICML2024	4.4	22.1	85.71	97.80	77.34	83.32	95.92	99.28	69.23	93.13	92.66	97.84
VMamba-s		ICML2024	9.0	43.7	85.44	97.79	74.64	81.27	96.43	99.37	69.30	93.20	87.36	94.77
Ours		Ms-Mamba-t	-	0.64	4.32	88.41	98.29	87.30	93.49	97.31	99.60	72.14	94.31	98.75
	Ms-Mamba-s	-	0.76	4.97	87.06	98.24	86.05	92.31	97.13	99.49	73.01	94.40	98.00	99.78
	Ms-Mamba-b	-	1.59	8.39	87.33	98.17	87.80	94.17	97.14	99.48	70.53	93.50	96.85	99.64

two branches after layer normalization. This process can be formulated as follows:

$$Map_{k1}, Map_{k2} = LN(Map_x) \quad (1)$$

where $LN(\cdot)$ denotes the layer normalization process. In the first branch, the input Map_{k1} passes through a linear layer and a SiLU activation function, producing the output map Map'_{k1} . In the second branch, the input Map_{k2} goes through a linear layer, DWConv, and a SiLU activation function. It then passes through a 2D selective scanning (SS2D) module for further feature extraction. Finally, the feature map undergoes normalization, producing the output Map''_{k2} . Next, the feature maps from the two branches are fused through element-wise product, resulting in the feature Map_k . Lastly, it passes through the Partially Selected Feed-forward Network (PSFFN) for efficient selective receptive field extraction, while concatenating the residual with the original input, yielding the final output of the ARVSS Block: Map_G . This process is defined as follows:

$$Map'_{k1} = SiLU(Linear(Map_{k1})) \quad (2)$$

$$Map'_{k2} = DWConv(Linear(Map_{k2})) \quad (3)$$

$$Map''_{k2} = LN(SS2D(SiLU(Map'_{k2}))) \quad (4)$$

$$Map_k = Map'_{k1} \otimes Map''_{k2} \quad (5)$$

$$Map_G = Map_x \oplus PSFFN(Map_k) \quad (6)$$

Where $Linear(\cdot)$ represents processing using a linear layer, $SS2D(\cdot)$ denotes 2D selective scanning, $DWConv(\cdot)$ represents depth-wise separable convolution, $SiLU(\cdot)$ is the SiLU activation function, \otimes represents element-wise product, \oplus represents element-wise addition, and $PSFFN(\cdot)$ denotes

processing through the Partially Selected Feed-forward Network.

Partially Selected Feed-Forward Network. To further enhance Mamba’s ability to extract local features, we proposed a novel Partially Selected Feed-Forward Network (PSFFN), replacing the final linear layer in the ARVSS Block. As shown in Figure 1 (f), we primarily used PWConv and efficient partially depth-wise separable convolution (PDWConv) to complete the feed-forward feature extraction. Specifically, assuming the input feature is $X' \in R^{H \times W \times C}$, it first passes through PWConv to reduce the channel dimension, followed by the SiLU activation function, resulting in X' . Next, we split the input feature along the channel into two groups, with one group occupying 1/4 of the original channels and the other 3/4, producing outputs $X'_1 \in R^{H \times W \times \frac{C}{4}}$ and $X'_2 \in R^{H \times W \times \frac{3C}{4}}$. Then, PDWConv and SiLU further extract features from X'_1 , resulting in output X''_1 . Finally, the PSFFN employs channel concatenation to restore the size of the channel dimension, while channel shuffling is used to shuffle the feature map on the channel dimension to avoid information loss between channels. This process is defined as follows:

$$X' = SiLU(PWConv(X)) \quad (7)$$

$$X'_1, X'_2 = Split(X') \quad (8)$$

$$X''_1 = SiLU(PDWConv(X'_1)) \quad (9)$$

$$Y = Shuffle(F_{cat}(X''_1, X'_2)) \quad (10)$$

where $PWConv(\cdot)$ denotes point-wise convolution, $Split(\cdot)$ denotes channel splitting, $PDWConv(\cdot)$ denotes efficient partially depth-wise separable convolution, $Shuffle(\cdot)$ denotes channel shuffle, and $F_{cat}(\cdot)$ denotes

channel-concatenation. By introducing PSFFN, the ARVSS Block can adaptively adjust the global features output by SS2D, reducing parameters and improving the model’s perception of detailed features.

C. Modulation Interaction Feature Aggregation Module

Since the visual state space block focuses on capturing global features, we introduced parallel Conv branches and the PSFFN to incorporate local features. However, these alone cannot effectively fuse global and local features. Therefore, we introduced the Modulation Interaction Feature Aggregation (MIFA) module, which operates between the two branches to modulate and adjust the features F_L and F_G . Specifically, by calculating the global feature maps and local feature maps W_L and W_G , the two input branches are re-weighted. The calculation process can be formulated as follows:

$$W_G = \delta(GELU(PWConv(F_L))) \quad (11)$$

$$W_L = \delta(RELU(PWConv(F_G))) \quad (12)$$

where $GELU(\cdot)$ is the GELU activation function, $ReLU(\cdot)$ is the ReLU activation function, and $\delta(\cdot)$ denotes the Sigmoid activation function. Next, through the matrix dot product, the global and local feature maps are applied to their respective branches. Channel concatenation and ECA attention [33] are then used to complete the feature map aggregation. This process can be formulated as follows:

$$Map_{fusion} = ECA(F_{cat}((W_G \otimes F_L), (W_L \otimes F_L))) \quad (13)$$

Here, Map_{fusion} represents the final output of the MIFA module and $ECA(\cdot)$ denotes ECA Attention.

III. EXPERIMENTS

A. Datasets and Implementation Details

To validate the model’s performance, we selected five public medical image datasets: the Retinal Pigment Epithelium (RPE) Cell dataset, minimalist histopathology image analysis dataset (MHIST), the Malaria Cell Image dataset (SARS), TissueMNIST, and MedFM Colon [34]–[38]. The RPE dataset comprises 1,862 images of retinal pigment epithelium cells, classified into four categories. The SARS dataset includes 27,558 images of malaria cells, divided into two categories. MHIST contains 3,152 images of colorectal polyps for binary classification. The MedMF Colon dataset classifies tumor tissues in colonoscopy pathology slides, consisting of 10,009 pathological tissue patches from 396 colon cancer patients. TissueMNIST features 236,386 images of human kidney cortex cells, categorized into eight groups. All datasets were split into training, validation, and test sets in a 6:2:2 ratio.

We implemented our Microscopic-Mamba with PyTorch 2.0.0 and trained it on an NVIDIA RTX 3090 (24GB), processing 200 epochs with a batch size of 16. We employed the Adam optimizer with an initial learning rate of 0.0001, a weight decay of $1e-4$, and Cross-Entropy Loss to optimize the model parameters. Additionally, we incorporated a cosine annealing learning rate decay strategy and an early stopping strategy with a 10-epoch warm-up period during training.

TABLE II
QUANTITATIVE COMPARISONS WITH DIFFERENT COMBINATIONS OF THE PSFFN AND MIFA

PSFFN	MIFA	Params	RPE Data			MHIST		
			OA	Pre	AUC	OA	Pre	AUC
×	×	4.86	87.14	88.21	97.32	84.79	84.56	91.10
✓	×	4.30	87.87	89.24	98.28	86.21	85.99	89.51
×	✓	4.89	87.60	89.28	98.15	85.74	85.92	91.83
✓	✓	4.32	88.41	89.68	98.29	87.30	87.67	93.49

TABLE III
EFFECT OF THE PARALLEL VSSM MECHANISM

Parallel	Params	RPE Data			MHIST		
		OA	Pre	AUC	OA	Pre	AUC
×	8.83	87.60	88.71	98.28	86.05	85.83	91.30
✓	4.32	88.41	89.68	98.29	87.30	87.67	93.49

B. Comparison with SOTA Models

Table I shows the comparison between our method and state-of-the-art methods. These methods include CNN-based, Transformer-based, Hybrid-CNN-Transformer-based, and Mamba-based approaches. From Table I, it can be seen that Microscopic-Mamba achieved the best results in terms of Params, GMACs, Overall Accuracy (OA), and Area Under the Curve (AUC) across five datasets.

C. Ablation Study

As shown in Table II, we conducted detailed ablation experiments on the RPE and MHIST datasets. The results indicate that both the MIFA and PSFFN modules contribute to improved model performance while maintaining lower parameter counts. The best results were achieved when MIFA and PSFFN were used together. Additionally, as shown in Table III, the introduced parallel VSSM mechanism not only reduced model complexity but also improved performance by incorporating multi-scale interactions.

IV. CONCLUSION

In this paper, we propose a new network based on Mamba: Microscopic-Mamba. It eases the computational constraints in real-world medical scenarios with lower computational complexity. Microscopic-Mamba features a dual-branch structure composed of SSM and CNN. We introduced the Modulation Interaction Feature Aggregation (MIFA) module to modulate and aggregate global-local features from both branches efficiently. Additionally, we replaced the final linear layer in the Mamba module with a Partially Selected Feed Forward Network (PSFFN) to further enhance Mamba’s local perception capabilities. Meanwhile, we introduced a parallel VSSM mechanism, maintaining low computational complexity while enhancing information interaction between channels. Experimental results demonstrate that our proposed method outperforms other state-of-the-art methods on five public datasets. We believe that our specialized Mamba architecture design can offer new perspectives for MIC.

REFERENCES

- [1] X. Ying and T. M. Monticello, "Modern imaging technologies in toxicologic pathology: An overview," *Toxicologic pathology*, vol. 34, no. 7, pp. 815–826, 2006.
- [2] F. Merchant and K. Castleman, *Microscope image processing*. Academic press, 2022.
- [3] Z. Liu, L. Jin, J. Chen, Q. Fang, S. Ablameyko, Z. Yin, and Y. Xu, "A survey on applications of deep learning in microscopy image analysis," *Computers in Biology and Medicine*, vol. 134, p. 104523, 2021. [Online]. Available: <https://www.sciencedirect.com/science/article/pii/S0010482521003176>
- [4] N. Sengar, R. Burget, and M. K. Dutta, "A vision transformer based approach for analysis of plasmodium vivax life cycle for malaria prediction using thin blood smear microscopic images," *Computer Methods and Programs in Biomedicine*, vol. 224, p. 106996, 2022.
- [5] S. Kumar, T. Arif, A. S. Alotaibi, M. B. Malik, and J. Manhas, "Advances towards automatic detection and classification of parasites microscopic images using deep convolutional neural network: methods, models and research directions," *Archives of Computational Methods in Engineering*, vol. 30, no. 3, pp. 2013–2039, 2023.
- [6] L. D. Nguyen, D. Lin, Z. Lin, and J. Cao, "Deep cnns for microscopic image classification by exploiting transfer learning and feature concatenation," *2018 IEEE international symposium on circuits and systems (ISCAS)*, pp. 1–5, 2018.
- [7] M. Masud, H. Alhumyani, S. S. Alshamrani, O. Cheikhrouhou, S. Ibrahim, G. Muhammad, M. S. Hossain, and M. Shorfuzzaman, "Leveraging deep learning techniques for malaria parasite detection using mobile application," *Wireless Communications and Mobile Computing*, vol. 2020, no. 1, p. 8895429, 2020.
- [8] T. Huang, L. Huang, S. You, F. Wang, C. Qian, and C. Xu, "Lightvit: Towards light-weight convolution-free vision transformers," *arXiv preprint arXiv:2207.05557*, 2022.
- [9] W. Wang, E. Xie, X. Li, D.-P. Fan, K. Song, D. Liang, T. Lu, P. Luo, and L. Shao, "Pyramid vision transformer: A versatile backbone for dense prediction without convolutions," *ICCV*, pp. 568–578, 2021.
- [10] Z. Tu, H. Talebi, H. Zhang, F. Yang, P. Milanfar, A. Bovik, and Y. Li, "Maxvit: Multi-axis vision transformer," *ECCV*, 2022.
- [11] Y. Li, G. Yuan, Y. Wen, J. Hu, G. Evangelidis, S. Tulyakov, Y. Wang, and J. Ren, "Efficientformer: Vision transformers at mobilenet speed," *NeurIPS*, vol. 35, pp. 12934–12949, 2022.
- [12] Z. Zhang, H. Wu, H. Zhao, Y. Shi, J. Wang, H. Bai, and B. Sun, "A novel deep learning model for medical image segmentation with convolutional neural network and transformer," *Interdisciplinary Sciences: Computational Life Sciences*, vol. 15, no. 4, pp. 663–677, 2023.
- [13] R. E. Kalman, "A new approach to linear filtering and prediction problems," *Journal of Basic Engineering*, 1960.
- [14] D. Y. Fu, T. Dao, K. K. Saab, A. W. Thomas, A. Rudra, and C. Ré, "Hungry Hungry Hippos: Towards language modeling with state space models," *ICLR*, 2023.
- [15] A. Gupta, A. Gu, and J. Berant, "Diagonal state spaces are as effective as structured state spaces," *NeurIPS*, vol. 35, pp. 22982–22994, 2022.
- [16] A. Gu and T. Dao, "Mamba: Linear-time sequence modeling with selective state spaces," *arXiv preprint arXiv:2312.00752*, 2023.
- [17] Z. Xing, T. Ye, Y. Yang, G. Liu, and L. Zhu, "Segmamba: Long-range sequential modeling mamba for 3d medical image segmentation," *arXiv preprint arXiv:2401.13560*, 2024.
- [18] J. Hao, L. He, and K. F. Hung, "T-mamba: Frequency-enhanced gated long-range dependency for tooth 3d cbct segmentation," *arXiv preprint arXiv:2404.01065*, 2024.
- [19] G. Yang, K. Du, Z. Yang, Y. Du, Y. Zheng, and S. Wang, "Cmvim: Contrastive masked vim autoencoder for 3d multi-modal representation learning for ad classification," *arXiv preprint arXiv:2403.16520*, 2024.
- [20] Z. Liu, H. Mao, C.-Y. Wu, C. Feichtenhofer, T. Darrell, and S. Xie, "A convnet for the 2020s," in *CVPR*, 2022, pp. 11976–11986.
- [21] A. Wang, H. Chen, Z. Lin, J. Han, and G. Ding, "Repvit: Revisiting mobile cnn from vit perspective," in *CVPR*, 2024, pp. 15909–15920.
- [22] P. K. A. Vasu, J. Gabriel, J. Zhu, O. Tuzel, and A. Ranjan, "An improved one millisecond mobile backbone," *arXiv preprint arXiv:2206.04040*, 2022.
- [23] W. Wang, E. Xie, X. Li, D.-P. Fan, K. Song, D. Liang, T. Lu, P. Luo, and L. Shao, "Pvtv2: Improved baselines with pyramid vision transformer," *Computational Visual Media*, vol. 8, no. 3, pp. 1–10, 2022.
- [24] Y. Lee, J. Kim, J. Willette, and S. J. Hwang, "Mpvit: Multi-path vision transformer for dense prediction," in *CVPR*, 2022, pp. 7287–7296.
- [25] X. Chu, Z. Tian, Y. Wang, B. Zhang, H. Ren, X. Wei, H. Xia, and C. Shen, "Twins: Revisiting the design of spatial attention in vision transformers," in *NIPS*, 2021. [Online]. Available: <https://openreview.net/forum?id=5KT1VBkzSRx>
- [26] A. Dosovitskiy, L. Beyer, A. Kolesnikov, D. Weissenborn, X. Zhai, T. Unterthiner, M. Dehghani, M. Minderer, G. Heigold, S. Gelly *et al.*, "An image is worth 16x16 words: Transformers for image recognition at scale," *arXiv preprint arXiv:2010.11929*, 2020.
- [27] P. K. A. Vasu, J. Gabriel, J. Zhu, O. Tuzel, and A. Ranjan, "Fastvit: A fast hybrid vision transformer using structural reparameterization," in *ICCV*, 2023, pp. 5785–5795.
- [28] A. Shaker, M. Maaz, H. Rasheed, S. Khan, M.-H. Yang, and F. S. Khan, "Swiftformer: Efficient additive attention for transformer-based real-time mobile vision applications," in *ICCV*, 2023, pp. 17425–17436.
- [29] K. Li, Y. Wang, J. Zhang, P. Gao, G. Song, Y. Liu, H. Li, and Y. Qiao, "Uniformer: Unifying convolution and self-attention for visual recognition," *arXiv preprint arXiv:2201.09450*, 2022.
- [30] W. Lin, Z. Wu, J. Chen, J. Huang, and L. Jin, "Scale-aware modulation meet transformer," *arXiv preprint arXiv:2307.08579*, 2023.
- [31] Y. Yue and Z. Li, "Medmamba: Vision mamba for medical image classification," *arXiv preprint arXiv:2403.03849*, 2024.
- [32] Y. Liu, Y. Tian, Y. Zhao, H. Yu, L. Xie, Y. Wang, Q. Ye, and Y. Liu, "Vmamba: Visual state space model," *arXiv preprint arXiv:2401.10166*, 2024.
- [33] Q. Wang, B. Wu, P. Zhu, P. Li, W. Zuo, and Q. Hu, "Eca-net: Efficient channel attention for deep convolutional neural networks," in *CVPR*, 2020, pp. 11534–11542.
- [34] L. Nanni, M. Paci, F. L. Caetano dos Santos, H. Skottman, K. Juuti-Uusitalo, and J. Hyttinen, "Texture descriptors ensembles enable image-based classification of maturation of human stem cell-derived retinal pigmented epithelium," *PLoS One*, vol. 11, no. 2, p. e0149399, 2016.
- [35] H. Yu, F. O. Mohammed, M. Abdel Hamid, F. Yang, Y. M. Kassim, A. O. Mohamed, R. J. Maude, X. C. Ding, E. D. Owusu, S. Yerlikaya *et al.*, "Patient-level performance evaluation of a smartphone-based malaria diagnostic application," *Malaria Journal*, vol. 22, no. 33, 2023. [Online]. Available: <https://doi.org/10.1186/s12936-023-04446-0>
- [36] J. Yang, R. Shi, D. Wei, Z. Liu, L. Zhao, B. Ke, H. Pfister, and B. Ni, "Medmnist v2-a large-scale lightweight benchmark for 2d and 3d biomedical image classification," *Scientific Data*, vol. 10, no. 1, p. 41, 2023.
- [37] J. Wei, A. Suriawinata, B. Ren, X. Liu, M. Lisovsky, L. Vaickus, C. Brown, M. Baker, N. Tomita, L. Torresani *et al.*, "A petri dish for histopathology image analysis," in *AIM*. Springer, 2021, pp. 11–24.
- [38] D. Wang, X. Wang, L. Wang, M. Li, Q. Da, X. Liu, X. Gao, J. Shen, J. He, T. Shen *et al.*, "A real-world dataset and benchmark for foundation model adaptation in medical image classification," *Scientific Data*, vol. 10, no. 1, p. 574, 2023.